Absorption spectroscopy on the argon first excited state in an expanding thermal arc plasma

A. J. M. Buuron, D. K. Otorbaev, M. C. M. van de Sanden, and D. C. Schram
Department of Physics, Eindhoven University of Technology, P.O. Box 513, 5600 MB Eindhoven, The Netherlands
(Received 14 March 1994)

Absorption spectroscopy was used to determine the density of argon atoms in the first excited state in an expanding cascaded arc plasma jet, in order to estimate their relative contribution to the energy exchange processes in plasma jets used for deposition purposes. In the spectroscopic setup a stagnant cascaded arc was used as a high-intensity continuum light source and optical multichannel detection was employed. Measurements were done on the strong Ar($3p^5 4s$-$3p^5 4p$) radiative transitions in the range of 794.8–852.1 nm. An efficient numerical method for obtaining radial density and temperature profiles, using line of sight integration instead of Abel inversion, has been developed. For a purely argon plasma the Ar($3p^5 4s$) metastable and resonant state densities lie in the range of 10^{18}–10^{16} m^{-3} at a chamber pressure of 40 Pa. The observed decay of the densities in axial direction was also modeled using the quasistationary continuity equation. It appears that the population density of the argon 4*s* states is determined mainly by the production due to the three-particle recombination and by the partial trapping of resonance radiation. The total densities of the argon first excited state are approximately a factor of 10 lower than the argon ion densities, so the contribution of these states to energy exchange processes in expanding cascaded arc deposition plasmas is limited compared to that of the argon ions.

PACS number(s): 52.25.Rv, 07.65.Eh, 52.25.Fi, 02.70.−c

I. INTRODUCTION

In the past, the expanding cascaded arc plasma jet has been the subject of extensive studies [1–3]. An important application of the method is the deposition of layers of carbon [4]. To this end, hydrocarbons are admixed into the argon carrier gas. It has been postulated that the argon ions play a major role in the production of active carbon species through multiple charge transfers from the argon ions to the hydrocarbon radicals, followed by dissociative recombinations of the radicals [3]. The question has risen whether the argon Ar($3p^5 4s$) metastable states (in the following denoted as argon 4*s* states) can also play an important role through excitation energy transfer to the admixed species. The rate coefficients for charge transfer from argon ions and excitation energy transfer from argon 4*s* metastables to admixed species are often of the same order, $\simeq 10^{-15}$ $m^3 s^{-1}$ [5,6]. Therefore, the densities of the argon ion and argon 4*s* densities in the expanding plasma jet should be compared. Ion densities in argon and argon-methane plasmas have been determined in the past using emission spectroscopy [3], Thomson scattering [7], and probe measurements [8]. In order to determine the densities of species which are not observable in emission spectroscopy, an absorption spectroscopy setup was developed. In the present study, measurements on the metastable and resonant argon 4*s* states in a purely argon plasma have been carried out. In the experimental setup, a stagnant cascaded arc is employed as a high-intensity continuum light source. Using a special optical system, lateral scans of the expanding jet were made on various axial positions. In Ref. [9] a method was presented for solving the radial density profiles assuming a uniform absorption spectral line profile over the line of sight. The data were analyzed using the curves of growth [10], followed by a conventional deconvolving Abel inversion method. When the profile of the absorption line changes along the observation path, this method is not accurate. In the supersonic and the shock region of the expanding plasma, interesting features are averaged out employing this method. As the medium is inhomogeneous, besides the radial variation of the absorbing particles density also the variations of the heavy particle temperature and additionally the electron density (in the case of Stark broadening of the spectral line) influence the measured absorption and hence enter into the Abel equations.

In the present study an efficient numerical method is used in order to solve this complicated problem, based on a reverse approach, using integration over a line of sight. One may adopt a radial profile for the densities and temperatures in the plasma beam and calculate the expected values of the total absorption over a line of sight. Consequently, by fitting the calculated values to the measured values in a least-squares procedure, the parameters of the profiles can be determined. In other words, we calculate the analogies of the curves of growth for the particular inhomogeneous medium under investigation. In principle this method is also suited for the calculation of solutions of the equation of radiative transfer in inhomogeneous media such as escape factors. Furthermore, in contrast to the noise amplifying character of Abel inversion techniques, this method reduces the influence of measurement noise in the final results.

In the supersonic region of the expanding plasma, the densities of the argon 4*s* states on the axis of the expanding plasma jet can also be modeled using a quasi-one-dimensional approach for solving the mass balance equation in the expansion. For modeling the axial densities in the subsonic region, a simple local balance can be used.

II. EXPERIMENT

A. Optical absorption spectroscopy

Consider a beam of parallel light with spectral intensity I_ν, passing through a (one-dimensionally) inhomogeneous absorbing medium. The intensity on location x in the medium is then described by [11]

$$\frac{dI_\nu(x)}{dx} = -k_\nu(x) I_\nu(x) , \tag{1}$$

where $k_\nu(x)$ is the local spectral absorption coefficient in the medium. The integrated absorption coefficient is given by [12]

$$\int_0^\infty k_\nu(x) d\nu = \frac{\lambda_0^2 g_k}{8\pi g_i} n_i(x) A_{ki} \left[1 - \frac{g_{in_k}(x)}{g_k n_i(x)} \right] , \tag{2}$$

with $n_i(x)$ and $n_k(x)$ the local densities of the particles in the lower and upper levels, respectively, and g_i and g_k the statistical weights of these levels. A_{ki} is the Einstein transition probability for spontaneous emission. In most cases the ratio $n_k(x)/n_i(x)$ can be neglected. It appears that for determining n_i one is more interested in the total absorption $\mathcal{A}_g$ than in the spectral absorption coefficient. The total absorption is defined as the ratio of the absorbed energy and the incident intensity [12]. If the light source emits a continuum with uniform spectral intensity I_0, the absorbed energy will be $I_0 \int_0^\infty \{1 - \exp\{-\int_0^l k_\nu(x) dx\}\} d\nu$ and

$$\mathcal{A}_g = \int_0^\infty \left[1 - \exp\left[-\int_0^l k_\nu(x) dx \right] \right] d\nu , \tag{3}$$

with l the path length through the medium. The optical depth is defined as $\int_0^l k_0(x) dx$, with k_0 the value of the spectral absorption coefficient in the line center. Equation (3) expresses the relation between the measured total absorption $\mathcal{A}_g$ and the density of the absorbing particles integrated over the line of sight. In general, this relation is nonlinear and is expressed by a "curve of growth" [10,11,13]. The curve of growth depends on the ratio a of the Lorentzian and Gaussian fractions of the spectral line, i.e., on the line broadening mechanisms in the plasma.

B. The expanding cascaded arc plasma

In Fig. 1 the entire experimental setup is shown. It comprises two cascaded arc sources, the first one serving as a particle source for generating the plasma jet expanding into a vacuum chamber and the second one serving as a light source in the spectroscopy system. The common feature of both sources is the generation of a thermal argon arc plasma in a channel built up by a stack of annular cascade plates. Depending on their specific purposes, the operating parameters for the two arcs are quite different. These are summarized in Table I. The arc as a particle source operates on a large argon flow and the exit of the arc channel (the nozzle) is connected to a vacuum chamber. In the nozzle a hydrocarbon gas can be injected, and by exchange processes from the argon to the injected species active (hydro)carbon radicals and ions are created. The particles expand supersonically into the vacuum chamber, pass through a shock region, and are transported subsonically toward the substrate where deposition takes place. With this method, the deposition rates are orders of magnitude higher than with diffusion governed plasma deposition methods. The application of the cascaded arc in a deposition setup is described in detail elsewhere [14–16].

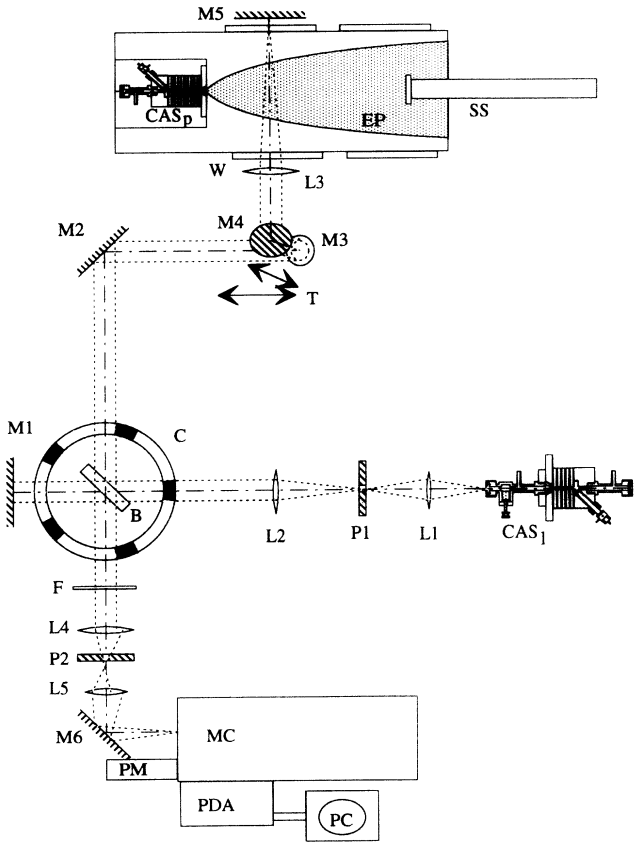

FIG. 1. The expanding cascaded arc plasma and the spectroscopy setup: CAS_I, cascaded arc light source; M, mirrors; L; quartz lenses; $P_{1,2}$, pinholes; B, beam splitter; C; chopper; T, translator; CAS_P, cascaded arc particles source; EP, expanding plasma; SS, movable substrate support; W, quartz window; F, order filter; MC, monochromator; PDA, photodiode array; PM, photomultiplier; PC, personal computer.

TABLE I. The operating parameters of the flowing arc as a particle source and the stagnant arc as a light source.

Operating parameter	Particle source	Light source
I_{arc} (A)	45	45
V_{arc} (V)	85	90
Φ_{Ar} ($cm^3 s^{-1}$)	58	0.05
p_{arc} (10^5 Pa)	0.3	3
$p_{chamber}$ (Pa)	40	
l_{arc} (mm)	60	42
R_{arc} (mm)	2	1
T_{arc} (eV)	1	1.5

C. The absorption spectroscopy setup

With the spectroscopy setup the densities of the argon metastables in the expanding plasma beam and their role in the exchange processes with the injected species can be studied. To this end the expanding plasma is exposed to a beam of light from the second cascaded arc, the light source [17,18]. This arc is a modified type of the arc as a particle source, especially designed for obtaining a continuous high-intensity light emission ranging from the far ir into the uv. This arc consists of a closed system operating on a high pressure and a low argon flow (cf. Table I). The source can also be used for infrared absorption measurements [19] and spectroscopic ellipsometry [20]. The intensity of the continuum radiation is only a factor of ~ 10 lower than according to Planck's law (with $T \simeq 14\,000$ K). In the spectral lines, the intensity approaches the value according to Planck and is of the order of 2×10^{14} W m^{-3} sr^{-1} at 800 nm. In the light source, the Stark broadening of the argon lines is very large (several tenths of nanometers) compared to the widths of the lines under investigation and we can consider the source as a continuum source in the vicinity of the studied line. It has been verified that the intensity of the light incident on the plasma under investigation will not perturb it significantly. The excitation rate of the $4s$ state, with density n_{4s}, by the incident light is of the order of $10^3 n_{4s}$ s^{-1} [21] while that by electronic collisions (with an electron density of the order of 10^{19} m^{-3}) is of the order of $10^5 n_{4s}$ s^{-1} [22]. The intensity of the light transmitted through the plasma (I_t) is now measured in the following way: By the lenses $L1$ and $L2$ (focal lengths 75 and 400 mm, respectively) a beam of parallel light is created and passed on by the beam splitter (B). The way to mirror $M1$ is being blocked by the chopper C. The beam is passed on by the mirrors $M2$, $M3$, and $M4$ and focused by a lens $L3$ (focal length 780 mm), through the plasma, on the mirror $M5$. The mirror $M3$ and the mirror $M4$ together with lens $L3$ are transferable, which enables axial and lateral scanning. The light is reflected, passes the plasma once again, and is transmitted, through the order filter F, to the detection section. The beam is focused on the entrance slit of the monochromator by the optical system, consisting of the lenses $L4$ and $L5$; the focal lengths of these lenses are 400 and 75 mm, respectively. The detection volume has a diameter of ~ 1 cm on the plasma axis. Additionally necessary data are the source signal (I_s), the plasma emission (I_e), and the dark current of the detection system (I_d). By rotating the chopper one can alternately pass the intensities to be measured to the detection system, or block them. A calibration factor for the attenuation through the two branches of the optical system was obtained by taking the intensity ratio of the continuum radiation in the vicinity of the lines under study. The detection consists of a high resolution monochromator (dispersion 0.8 nm/mm at 500 nm) and a Peltier-cooled photodiode array, coupled to a personal computer. The photodiode array consists of 1024 elements (pixels). The entrance slit width of the monochromator was set at 25 μm, which is equal to the width of one pixel. The spectral width per pixel is approximately 17 pm. Computer controlling of the rotation of the chopper C and the translator T now enables continuous fast and automatic acquisition of data on several spectral lines simultaneously, on various axial and lateral positions. More information on this setup can be found in [21].

The application of a photodiode array in absorption spectroscopy experiments requires a careful analysis of the measured signal. The measured integrated relative absorption A_m (with intensities corrected for attenuation by the optical system) is given by

$$A_m = 1 - \frac{\int_{\text{app}} (I_t + I_e) - \int_{\text{app}} I_e}{\int_{\text{app}} (I_s + I_d) - \int_{\text{app}} I_d} , \tag{4}$$

where $\int_{\text{app}}$ denotes convolution of the intensities with the apparatus profile of the detection system, i.e., the monochromator and the diode array. Equation (4) can be transformed to [21]

$$A_m = \frac{1}{N \Delta \nu_{\text{pixel}}} \frac{\int_{\text{line}} I_{\text{abs}}(\nu) d\nu}{I_0} = \frac{1}{N \Delta \nu_{\text{pixel}}} \mathcal{A}_g , \tag{5}$$

with $\int_{\text{line}} I_{\text{abs}}(\nu) d\nu$ denoting integration of the absorbed intensity over the line profile and $\mathcal{A}_g$ the total absorption already defined in Sec. II A. N is the number of pixels over which the spectral line is spread by the apparatus profile. Of course, increasing the entrance slit width of the monochromator does not change the value of the total absorption but only that of the measured integrated relative absorption. The slit width enters the equation because the measured total (continuum) source intensity is proportional to the square of it and the measured total (line) absorption is only linearly proportional to it. The effect of the apparatus profile was taken into account by the following procedure. The exact value of N is not an integer. However, Eq. (5) is also valid if the number of pixels N is taken larger than the number over which the apparatus profile is spread. This supplies us with the following method for converting the measured integrated relative absorption values A_m to the total absorption values $\mathcal{A}_g$ without determining the apparatus profile (the number of pixels N) exactly: By integrating A_m over a sequence of values N, $\mathcal{A}_g$ results as the slope in a graph of $A_m \, \Delta\nu_{\text{pixel}}$ vs $1/N$.

D. Measurement condition

In Fig. 2 the studied section of the argon system and the selected spectral transitions are shown. The four argon $3p^5 4s$ states under investigation can be distinguished in two metastable states ($^3P_0$ and $^3P_2$, also denoted as s_3 and s_5, respectively) and two resonant states ($^1P_1$ and $^3P_1$, s_2 and s_4, respectively). By means of the photodiode array absorption measurements could be performed simultaneously on the eight spectral transitions depicted in Fig. 2. These lines were covered by selecting only two monochromator positions. In the figure the specific parameters of the studied spectral transitions are also given (adopted from [23]). Most of the lines have large transition probabilities. They were selected to obtain strong

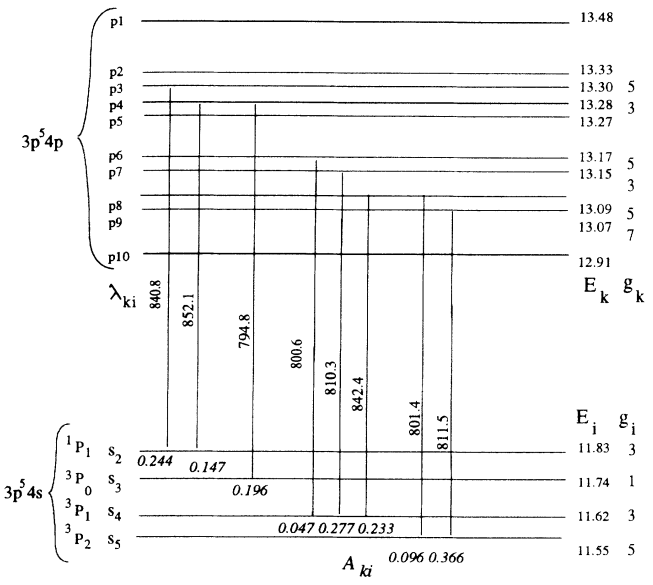

FIG. 2. The four argon $3p^5 4s$ states and the spectral transitions under investigation. Transition probabilities (A_{ki}, in 10^8 s^{-1}), statistical weights (g_i, g_k), wavelengths (λ_{ki}, in nm), and energies (E_i, E_k, in eV) are denoted in the figure.

absorption, leading to an acceptable signal-to-noise ratio. The measured integrated relative absorption values are in the order of 0.1–0.7 with an error of maximally ~0.05. The subsequent inaccuracy in the density determination cannot be determined analytically but can only be estimated at maximally ~50%. Taking into account the moderating effect of the actual convolution technique on the effect of the measurement noise in the final results, the inaccuracy in the final results may be much smaller.

Measurements on the densities of the argon 4s states were done for the reactor settings given in Table I, column 2. These are the standard settings also used in Thomson scattering experiments [7,24] and Fabry-Pérot line profile measurements [25]. There are six axial positions, 27, 47, 67, 87, 107, and 127 mm from the end of the channel of the cascaded arc (the beginning of the nozzle [26]). At each axial position, 45 lateral measurements were done, 2 mm apart from each other.

On the measurement positions the Lorentz fraction of the absorption line profiles can be neglected compared to the Gaussian fraction. This is justified as follows: The Doppler broadening in the expansion, with an argon heavy particle temperature of ~3000 K, is ~4 pm. The Stark broadening for the observed 4s-4p transitions, assuming a typical electron density of 10^{19} m^{-3}, is of the order of 4×10^{-3} pm [27]. The natural widths of the resonant 4s lines, with $A_{ki}=1.2\times10^8$ and 5.1×10^8 s^{-1}, can be calculated at about 5×10^{-4} and 2.5×10^{-3} pm, respectively [27]. Resonance broadening at 40 Pa and 3000 K is of the order of 10^{-4} pm [28]. Consequently the ratios of the Lorentzian and Gaussian fractions of the line profiles are of the order of 2×10^{-3}, in which case the effect of the Lorentzian fraction is very small for the moderate optical depths concerned, $\int_0^l k_0(x)dx \leq 100$. So in the data analysis we can adopt a purely Gaussian line profile, varying over the line of sight.

E. Convolution method for analyzing the absorption in inhomogeneous media

If the absorption line profile is not uniform over the line of sight, an efficient numerical method based on numerical integration of Eq. (3) can be applied. The principle of this convolution method is that the density and the temperatures profiles of the absorbing species are represented by physically reasonable functions. On the basis of the measured profiles of various species [2,16] it is justified to take for the density profiles a combination of Gaussian profiles, a narrow Gaussian (the plasma core) on top of a wide Gaussian as a background (representing metastable species in the recirculating background gas). A dip in the center of the density profiles, which is often observed in emission profiles of other species [2], can be simulated most conveniently by adding a third Gaussian with a negative area, to the total density profile. In Figs. 3(a) and 3(b) the geometry of the expanding beam and the adopted profiles are illustrated. For the temperature profile we adopt a narrow Gaussian with a width following the plasma core density width, on top of a low background temperature. We take centralized Gaussian functions of the form

$$f_i(r)=f_i(0)\exp\left[-\left[\frac{r}{\Delta r_i}\right]^2\right] \tag{6}$$

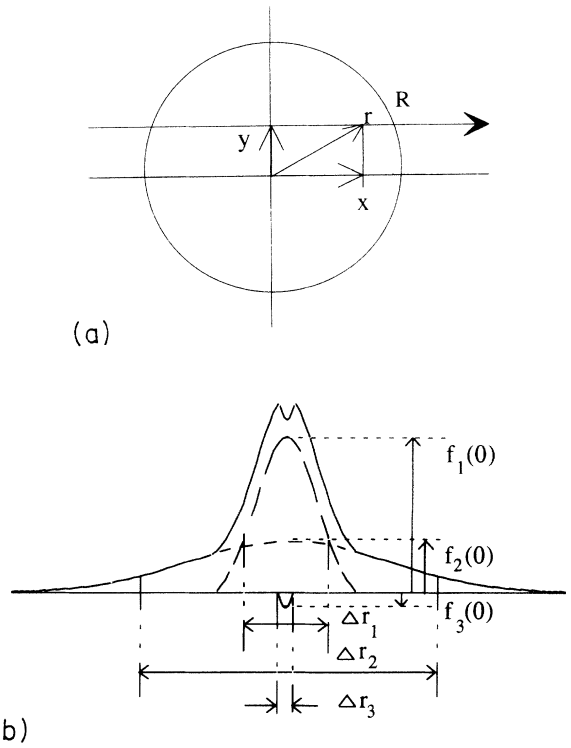

FIG. 3. (a) Geometry of a line of sight through the expanding plasma beam and (b) adopted density and temperature profiles over a line of sight.

with, as parameters, $f_i(0)$, the parameter (density or temperature) top value at the axis of the plasma, and Δr_i, the $1/e$ width of the ith Gaussian distribution; r is the radial coordinate, $r=\sqrt{x^2+y^2}$, with x the coordinate along the line of sight, which is taken at a height y, the lateral coordinate. So the number of independent parameters is two times the number of Gaussian functions plus two temperature parameters.

Using these prescribed temperature and density profiles, at each point (x,y) the absorption line profile of $k_\nu(r(x,y))$ is defined and $k_0(r(x,y))$ can easily be calculated (remember that the spectral line profile is also a Gaussian determined by the Doppler broadening. Equation (3) can now be integrated over the line of sight and per frequency channel. To this end, the line of sight has to be divided in a large number of small steps (250 steps of 2 mm), giving sufficient resolution of the density and temperature profiles. The total absorption upon traversing (in our case two times) the plasma can now be obtained by integrating over all frequency channels. It appears that 30 channels of $\frac{1}{10}$ of the Doppler line width, covering the profile over three times this width, is sufficient to keep the error in the integrated area less than 1%. Numerically, the most convenient way for obtaining the integrated absorption is to determine the frequency step by the smallest Doppler width (at the plasma edge) and then, going to the center, increase the number of steps proportionally to the Doppler width, as illustrated in Fig. 4. This procedure was carried out for each lateral position and the calculated values can be fitted to the measured integrated absorption values using a nonlinear least-squares parameter fit procedure. In this way optimum values for the parameters of the densities and temperatures profiles can be obtained. As a measure for the fit quality the following least-squares sum was used:

$$\chi^2=\frac{1}{N_y}\sum_{1}^{N_y}(A_{m,y}-A_{f,y})^2 , \tag{7}$$

with $A_{m,y}$ and $A_{f,y}$ the measured and fitted total absorption, respectively, on lateral position y and N_y the number of lateral data points. No weighing was applied because the photodiode array noise was the predominant (absolute) noise source.

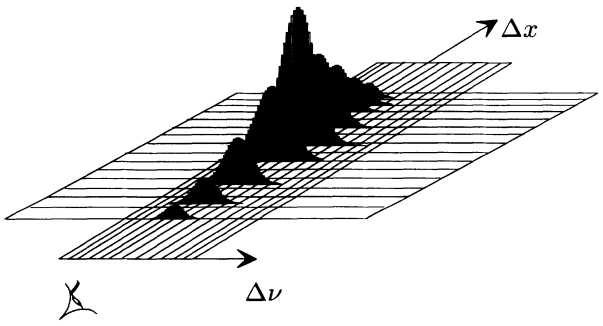

FIG. 4. Grid for integrating the absorption over the frequency ν and over a line of sight (with running coordinate x).

III. RESULTS AND DISCUSSION

A. Effect of the temperature on the density determinations and optimization of the fit procedure

In Ref. [9] it was already found that the results of the analysis of the measured absorption data on spectral lines of various strengths are sensitive to the heavy particle temperature in various degrees. This is caused by the nonlinear relationship between total absorption and density; an increasing linewidth reduces the amount of loss in measured absorption due to saturation in the top of the profile. With the present method, this difference in sensitivity can be used for a more accurate heavy particle temperature determination. As an example, the absorption data for the three lines coming from the s_4 substate were used. These three lines result in various optical depths $\int_0^l k_0(x)dx$. For the weak line (800.6 nm) the measured values of $\int_0^l k_0(x)dx$ are maximally about 4 (close to the nozzle). The measured absorption is weakly nonlinear with the density (integrated over the line of sight). For the two strong lines (810.3 and 842.4 nm) values of $\int_0^l k_0(x)dx$ of up to ~ 20 are obtained, and the measured absorption is strongly nonlinear with the density. The temperature profile can now be approximated by fitting the measured absorption values for these three lines simultaneously. For the density profile a combination of three Gaussian profiles was used, one of them with a negative top value in order to study the possible dip in the supersonic expansion region [2]. The density and temperature profiles obtained in this eight parameter fit procedure on the three spectral lines from the s_4 substate are represented in Figs. 5(a) and 5(b) as a contour plot and a three-dimensional map, respectively, up to the fourth axial position ($z=87$ mm).

In Fig. 5(a) it can be observed that for the region of 27–87 mm from the arc exit realistic values of the axial temperatures of about 3000 K were obtained. Temperature determinations for the positions $z=107$ and 127 mm were not possible, as the nonlinearity in the absorption is too small. In Fig. 6 the principle of the numerical procedure for the temperature determination for the locations close to the nozzle, using the three lines simultaneously, is illustrated. The variation of this best fit of the axial value of the density profiles with the axial value of the temperature profiles is shown for the three lines of level s_4 separately, for the two axial positions $z=27$ (solid symbols) and $z=127$ mm (open symbols). Regarding the locations close to the nozzle, it can be observed that for the two strong lines 810.3 and 842.4 nm the variations can be substantial (for the 842.4-nm line even greater than 100%), while for the weak line (800.6 nm) the effect is still small. The lack of a common crossing point of the three lines is due to the measurement inaccuracies. The least-squares procedure results in an optimum density value somewhere in the triangular crossing of the lines and in an axial temperature of about 2900 K. The spread of the three lines also provides an estimate for the uncertainty in the final s_4 density determination using the fit procedure, viz., $\pm 10\%$.

For the location ($z = 127$ mm) the measured absorption values are much lower and also obscured by the measurement inaccuracies. The resolved densities are almost independent of temperature and do not allow for a temperature optimum determination. This implies that for weak absorptions an accurate temperature determination is not possible, but also not necessary. For strong absorptions a temperature estimate is necessary and, on the other hand, feasible. For the first four axial positions the determined temperatures agree well with determinations from other experiments [25,29]. Heavy particle temperatures and rotational temperatures were determined to be around 3000 K at all of the six axial positions. So for the elaboration of all measurements, the fit procedure could be limited

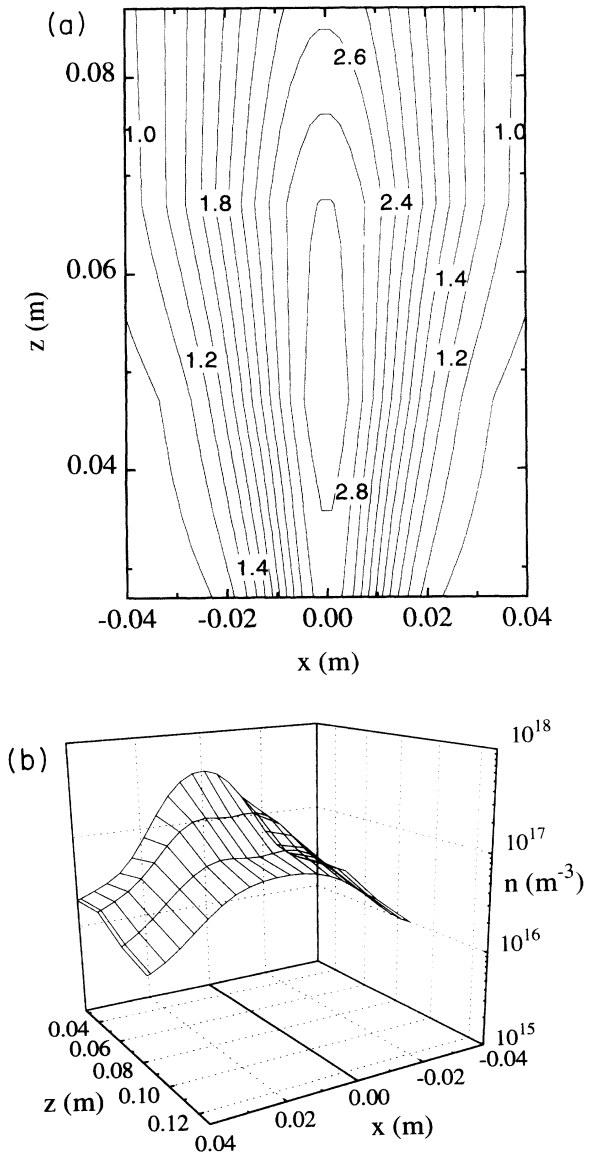

FIG. 5. (a) Heavy particle temperature contour plot (temperatures in 10^3 K) and (b) s_4 density map constructed by axial interpolation of the radial profiles on the first four axial positions as obtained in the optimal eight-parameter fit for the three s_4 lines simultaneously.

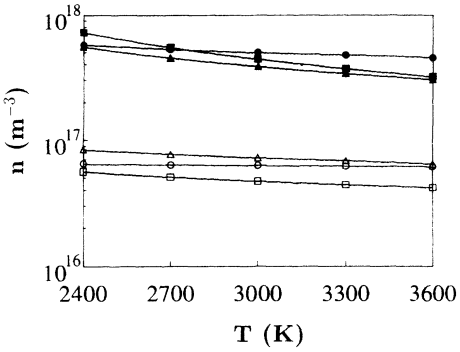

FIG. 6. Analysis of the top values of the radial density profiles for the three s_4 spectral lines obtained as a function of temperature, ●, ▲, and ■ for $\lambda = 800.6$, 810.3, and 842.4 nm, respectively, and for two axial positions: solid symbols, $z = 0.027$ m; open symbols, $z = 0.127$ m.

using only the parameters of the density profiles. For the temperature profile, a standard Gaussian profile was adopted with an axial top temperature of 3000 K, with a uniform (noncritical) background temperature of 700 K and with a width following that of the narrow density profile. Because of the above reasoning, the errors in the densities, due to the approximate temperatures used, will be small on all positions.

In the density map [Fig. 5(b)] only an insignificant central dip can be observed in the region from $z = 47$ to 67 mm. Repeating this fitting trial, using only two centralized Gaussian profiles gives a comparable fit quality as can be observed from the χ^2 values summarized in Table II. So it can be concluded that the absence of the axial dip in the density is real and that it is plausible to limit the modeling to two Gaussian profiles. So only four parameters have to be included in the fit procedure.

B. Absolute densities of the Ar($3p^5 4s$) states in the expanding argon plasma jet

The population densities of the four $4s$ substates were fitted to the measured absorption, simultaneously for the various available spectral lines on each substate: the three lines for the s_4 state, two lines for the s_2 and s_5 states, and one line for the s_3 state. The results of the densities of the four substates s_2, s_3, s_4, and s_5 as determined using the combination of two Gaussian density profiles and the standard Gaussian temperature profile (Sec. III A) are shown in Figs. 7(a)–7(d). As an example,

TABLE II. The least-squares values obtained in the fits with two and three Gaussian profiles in the supersonic expansion region.

z (m)	Two Gaussians units of (10^{-4})	Three Gaussians units of (10^{-4})
0.027	4.14	4.04
0.047	8.15	8.36
0.067	6.63	7.07
0.087	6.85	7.04

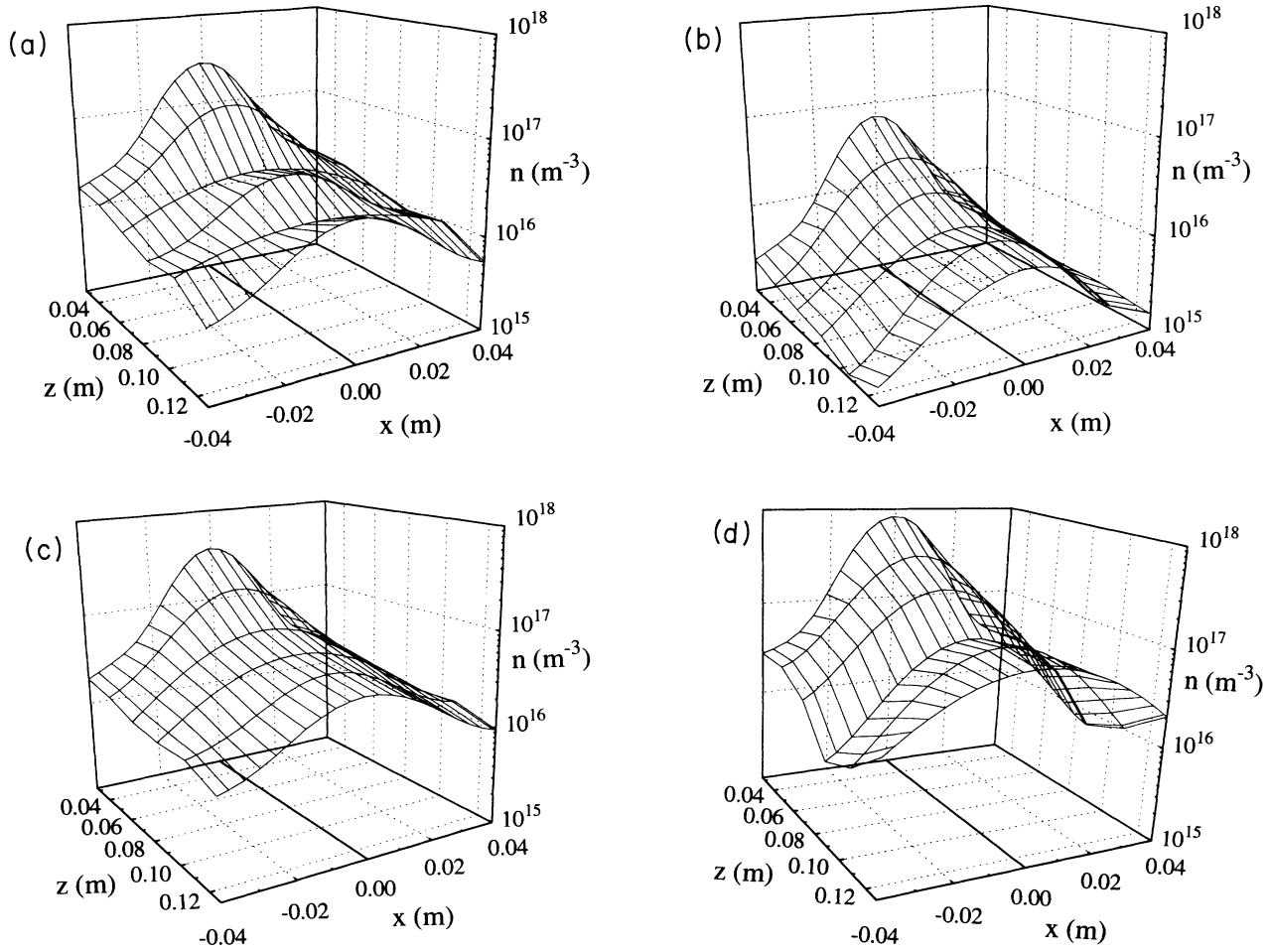

FIG. 7. Density maps of the four argon 4*s* substates in an argon plasma obtained by interpolation of the radial profiles on the six measurement positions: (a) s_2, (b) s_3, (c) s_4, and (d) s_5.

in Figs. 8(a)–8(c) the fit quality for the three lines coming from the s_4 substate is shown. It can be observed that for the first four positions the fits are indeed very good. For $z = 107$ and 127 mm, however, systematic errors of the profiles as a whole can be observed, due to the moderate signal-to-noise ratio (weak absorption). The alternating pixel noise of the array gave rise to an artificial positive or negative total absorption area, depending on the position of the line on the array.

The agreement with the data obtained earlier by the Abel inversion method [9] is reasonable, but now the density profiles are not averaged over the line of sight and do not exhibit mathematical artifacts. The actual Abel integration method has provided us with accurate density determinations on the plasma axis. In Fig. 9 these densities are depicted per statistical weights g_i(3, 1, 3, and 5, respectively), divided by the Boltzmann factor $\exp(-\Delta E/kT_e)$ (with ΔE with respect to the s_5 level), and using a value for the electron temperature T_e of 3000 K [2]. These normalized densities appear to be approximately equal, indicating a strong collisional coupling between the four states [22,30].

In Fig. 10 a map of the total density of 4*s* states over the entire cross section of the chamber is given (constructed by interpolation of the obtained radial density profiles on the six measurement positions). Although the lateral range of observation was only 9 cm in total, the radial extrapolation of the two Gaussians renders a physically reasonable picture of an increasingly wide region of a high density of 4*s* states, extending throughout the chamber at $z = 127$ mm. The total densities of the argon 4*s* state are a factor of ~ 10 lower than the ion densities [7]. So their contribution to exchange processes in deposition plasmas is limited compared to that of the ions. Using the Saha equation, these 4*s* densities imply underpopulation factors varying from values on the order of 10^{-6} in the supersonic expansion region, of 10^{-2} in the shock region, and of 10^{-5} in the subsonic region, expressing the nonequilibrium (recombining) character of the plasma.

C. Modeling of the population densities of the Ar($3p^5 4s$) states

1. General model

The measured axial argon 4*s* densities can be explained using a simple model. In the expansion the situation is

quasistationary and we can use the following mass balance:

$$\nabla\cdot(n_{4s}\mathbf{w}_{4s})=\left[\frac{\partial n_{4s}}{\partial t}\right]_S , \tag{8}$$

with n_{4s} and $\mathbf{w}_{4s}$ the density and the velocity of the $4s$ species. The source term $(\partial n_{4s}/\partial t)_S$ consists of several contributions. The most important in the case of an argon plasma are (ii) for the production, the three-particle recombination and

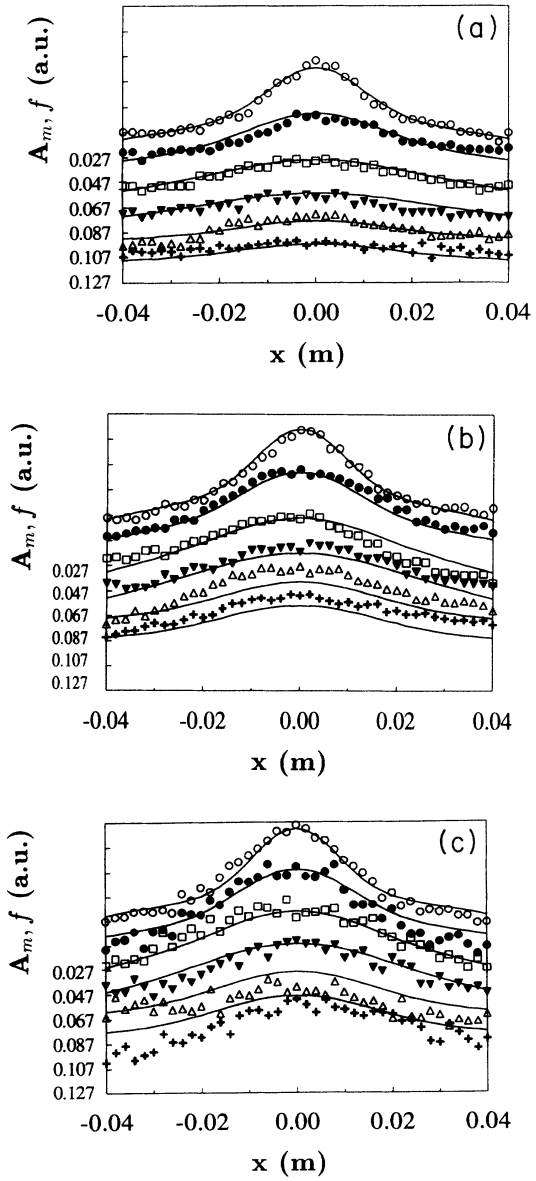

FIG. 8. Fit quality for the three s_4 lines obtained in the simultaneous fit (with fixed Gaussian temperature profiles): (a) 800.6 nm, (b) 810.3 nm, and (c) 842.4 nm. The zero axes for the various positions have been shifted to get a clearer image; the small figures on the left-hand axis indicate the zero level for the respective axial position. The symbols depict the measured absorption values: ○, ●, □, △, and + represent axial positions $z=0.027$, 0.047, 0.067, 0.087, 0.107, and 0.127 m, respectively.

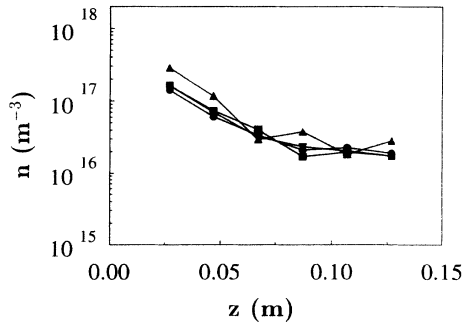

FIG. 9. Axial values of the densities of the $4s$ substates per statistical weight and corrected for the Boltzmann exponent: ▲, ●, ▼, ■ represent s_2, s_3, s_4, s_5, respectively.

$$Ar^+ + e + e \xrightarrow{K_{rec,3}} Ar_{4s} + e , \tag{9}$$

and (ii) for destruction, radiative decay (after $4s$ mixing) through the resonant states, followed by production by capture of the radiation

$$Ar_{4s} \xrightarrow{\Lambda A} Ar + h\nu , \tag{10}$$

with A and Λ the transition probability and the escape factor for resonance radiation, respectively. An uncertainty is the exact expression for the three-particle recombination coefficient [31,32,37,38]. We adopt the expression given by Biberman, Vorob'ev, and Yakubov [31]:

$$K_{rec,3}=C_{rec,3}T_e^{-9/2}\ (m^6 s^{-1}) , \tag{11}$$

with T_e the electron temperature. Here it is assumed that all three-particle recombinations cascade down to the $4s$ states. (This assumption is supported by the findings of Benoy *et al.* [32].) For the coefficient $C_{rec,3}$ a modified value of 3.3×10^{-21} $m^6K^{9/2}s^{-1}$ is adopted as recently found for an expanding thermal argon plasma by

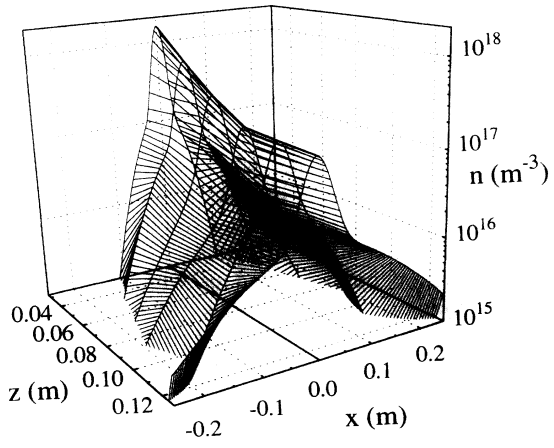

FIG. 10. Map displaying the total density of the argon $4s$ state over the entire cross section of the chamber, obtained by interpolation of the radial profiles on the six measurement positions.

van de Sanden, de Regt, and Schram [24]. The contributions of other reactions to production and destruction appear to be negligible.

2. *The subsonic expansion region*

An exact solution of Eq. (8) is readily obtained in the subsonic expansion region. Here the gradients are small and the entire left-hand side of Eq. (8) can be neglected. So in this region we can apply the following local balance between production and destruction:

$$K_{\mathrm{rec},3} n_e^3 = n_{4s} A_{4s\to 3p} \Lambda \ . \tag{12}$$

The escape factor Λ is a complicated function of the effective Voigt optical depth $k_0^V R$ (R is the radius of the plasma beam) (cf., e.g., [33]). For large optical depths the escape factor is mainly determined by the Lorentzian line wings. It has been deduced [22,34] that for $\Delta\lambda_L/\Delta\lambda_G \geq 100/k_0^V R$, with $\Delta\lambda_L$ and $\Delta\lambda_G$ the widths of the Lorentzian and Gaussian profile respectively, the dependence of Λ on the effective Voigt optical depth $k_0^V R$ can be expressed by taking only the Lorentz fraction of the line into account:

$$\Lambda(k_0^V R) = \left[\frac{4\pi c g_i \Delta\lambda_L}{g_k A_{ki} n_i \lambda_{ki}^4 \mu R} \right]^{1/2} , \tag{13}$$

with λ_{ki} the wavelength and c the light velocity. The subscripts k and i are again denoting upper and lower levels, respectively. n_i is the average value of the absorbing particles density; μ is a geometrical factor ($\mu \simeq 1.2$) [22]. For $1/k_0^V R < \Delta\lambda_L/\Delta\lambda_G < 100/k_0^V R$, Eq. (13) is valid in reasonable approximation. For resonance lines, the Gaussian Doppler broadening $\Delta\lambda_G$ is of the order of 10^{-3} nm. The Lorentzian broadening mechanisms in the expansion which we should consider are natural broadening, Stark broadening, and resonance broadening. The first has values of 5×10^{-7} and 2.5×10^{-6} nm, respectively, for the two lines. The Stark broadening $\Delta\lambda_{\mathrm{Stark}}$ is of the order of $5\times10^{-27}\ n_e$ nm [27], so in the subsonic part of the expansion, with $n_e \sim 10^{19}$ m^{-3}, $\Delta\lambda_{\mathrm{Stark}} < 10^{-7}$ nm and we may neglect it in first order approximation. Resonance broadening of the two resonant lines can be estimated at 4×10^{-9} and 1.5×10^{-8} nm [35] (with $n_0 \sim 10^{20}$ m^{-3}) and can also be neglected. So in the subsonic part of the expansion, natural broadening is the most important Lorentzian broadening mechanism. $k_0^V R$ is of the order $(1-5)\times10^3$ and Eq. (13) can be applied for approximating the escape factor. Substituting $\Delta\nu_L = 1/2\pi\tau = A/2\pi$ (for a resonance line) and $\Delta\lambda_L/\lambda = \Delta\nu_L/\nu$, Eq. (13) becomes

$$\Lambda(k_0^V R) = \left[\frac{2 g_i}{g_k n_i \lambda_{ki}^2 \mu R} \right]^{1/2} . \tag{14}$$

It appears that the escape factor for the resonant lines is independent of the transition probability A. Furthermore, it implies that the effective transition probabilities ΛA of the levels s_2 and s_4 remain linear in A and that the level with the largest transition probability (5.1×10^8 s^{-1}) represents the most important loss channel for the argon 4s states. Furthermore, because of the strong coupling between the four 4s sublevels, an average effective 4s transition probability of $\Lambda\times1.57\times10^8$ s^{-1} has to be used [22]. Using the values for n_e, T_e, and n_0 as obtained with Thomson scattering [7] and values of R from a quasi-one-dimensional expansion model [2], the axial dependence of the total 4s density in the subsonic expansion region is obtained. In Fig. 11 these data are depicted by the triangles. The agreement of the measured data with the model appears to be quite good, supporting the validity of the argon three-particle recombination coefficients of Ref. [24].

3. *The supersonic expansion region*

In the supersonic part transport has to be taken into account. In a good approximation, on the axis the expansion can be described by a quasi-one-dimensional expansion model [24,36]. Using

$$\nabla\cdot(n_{4s}\mathbf{w}_{4s}) = \frac{1}{S}\frac{d}{dz}(n_{4s}\mathbf{w}_{4s}S) \ , \tag{15}$$

in which S is the flux surface area and z the axial coordinate, Eq. (8) can be simplified to

$$2\frac{n_{4s}}{z} + \frac{dn_{4s}}{dz} + C_1 n_{4s} = f(z) \ , \tag{16}$$

with C_1 given by $A_{4s\to3p}\Lambda/w_{z,4s}$ and with $f(z)$ a function of z given by

$$f(z) = \frac{K_{\mathrm{rec},3}(z)}{w_{z,4s}} n_e^3(z) \ . \tag{17}$$

Under the condition of a spherical expansion, the dependence of n_e as well as that of the neutral particles density n_0 on the axial coordinate z can be expressed as follows [24,36]:

$$n_{e,0}(z) = n_{e,0}(z_0)\frac{z_{\mathrm{ref}}^2}{z^2} \ , \tag{18}$$

with z_0 the source point of the expansion and z_{ref} a normalization length of 1 mm. $K_{\mathrm{rec},3}$ is again given by Eq.

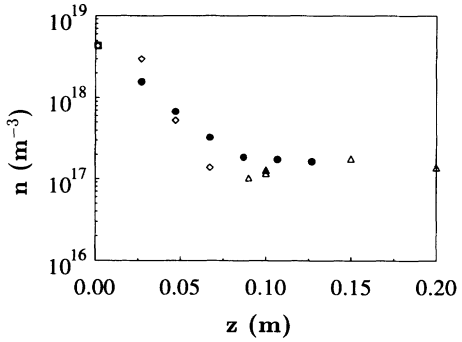

FIG. 11. Axial total densities of the 4s state n_{4s} as a function of the axial position z: ◇, △, and ● as calculated by the model of Eq. (16), as calculated by the model of Eq. (12), and from measured values, respectively. The symbol □ on position $z=0$ denotes the value of the 4s density, obtained using the Saha equation.

(11), but in the supersonic expansion $K_{\mathrm{rec},3}$ is also a function of z because T_e is a function of z. In [24] it was demonstrated that for the approximately adiabatically expanding plasma the following scaling law between $T_e(z)$ and $n_e(z)$ exists:

$$T_e^{\chi}(z)=C_0 n_e(z) , \tag{19}$$

in which χ has the value of $\frac{11}{3}$ and $C_0=2.2\times10^{-8}$ $\mathrm{m^3\,K^{11/3}}$. This relationship was shown to hold up to the shock. Using Eqs. (18) and (19), Eq. (17) can now be written uniquely as a function of z:

$$f(z)=C_2 z^{-39/11} , \tag{20}$$

in which C_2 is given by

$$C_2=C_0^{-27/22}\frac{C_{\mathrm{rec},3}}{w_{z,4s}} n_e(z_0) z_{\mathrm{ref}}^{39/11} . \tag{21}$$

The escape factor and the axial velocity $w_{z,4s}$ are also a function of z. Especially the dependence of Λ on z cannot easily be expressed analytically because several line broadening mechanisms come into play in various effectivities. In order not to complicate the problem any further we assume that the escape factor and the axial velocity are constant over the considered region. The average value of the escape factor is left as a degree of freedom and can be approximated by fitting the calculated densities to the measured densities. For the axial velocity in this supersonic expansion region an average value of 3000 $\mathrm{m\,s^{-1}}$ was adopted [24]. The homogeneous solution of Eq. (16) can easily be found to be a rapid exponential decay with C_1 as a coefficient, representing the effect of the expansion on the flux emerging from the source together with the loss by radiative decay to the ground state. The particular solution of Eq. (16), representing the effect of local production and destruction, combined with transport, cannot easily be found. We solved the equation using MAPLE software. The complete solution then reads

$$n_{4s}(z)=n_{4s}(z_0)\left[\frac{z_0}{z}\right]^2 e^{-C_1(z-z_0)} + \frac{\exp\left[-C_1 z\left[\int_{z_0}^{z}\frac{C_2 e^{C_1 z}}{z17/11}dz\right]\right]}{z^2} , \tag{22}$$

with z_0 the position where the following left-hand edge condition has to be applied. At $z_0=0$ (the arc channel exit), the solution should satisfy the local value for the 4s density. An estimate for this value can be obtained in the following way: In the arc the plasma is approximately in partial local thermal equilibrium. Using the Saha equation with the proper value of $n_e(z_0)=1.3\times10^{22}$ $\mathrm{m^{-3}}$ [24] and $T_e=1$ eV [39] the 4s density can be calculated to be $\approx4.3\times10^{18}$ $\mathrm{m^{-3}}$. The integral in Eq. (22) was calculated using an elementary numerical algorithm and in Fig. 11 the density values obtained in the supersonic expansion are depicted. For Λ a value of 10^{-3} was applied. It appears that the measured tendency of the gradual axial 4s decay is supported by the model. For a more exact treatment, also the axial dependence of the escape factor and of the axial velocity should be included in the model. Furthermore, Eq. (11) is extremely sensitive to small variations in T_e and n_e.

Analyzing the various contributions to the obtained densities more closely, it appears that the dominant production term is the substantial 4s production in the supersonic expansion by recombination, combined with the transport of these 4s states. The contribution of the 4s particles flux emerging out of the arc to the observed densities appears to be negligible. The observation that there is a large net production of 4s states in the supersonic expansion is also confirmed by considering the increase in the 4s particles flux. The diameter of the nozzle ($z=0$) is only 4 mm and the diameter of the plasma beam in the subsonic expansion is ~5 cm, while the velocities on both positions are in the same order and the densities only decrease by a factor of about 10.

IV. CONCLUSIONS

An efficient and relatively easy numerical method, based on line of sight integration, has been developed for analyzing spectroscopic absorption data for inhomogeneous media. The profile of the 4s densities in the expansion can be approximated adequately by a combination of two radial Gaussian profiles, a narrow one for the plasma core and a broad one for the background gas. Besides density profiles, in principle also profiles of other parameters (e.g., the heavy particle temperature) can be determined if the signal-to-noise ratio of the measurements is adequate.

The ability of the method to yield accurate axial density values is illustrated by the confirmation that on the axis the densities of the four 4s substates are thermally populated. This is caused by the rapid electronic collisional 4s substate mixing.

The total densities of the argon 4s states are a factor of ~10 lower than the ion densities so their contribution to exchange processes in expanding arc deposition plasmas is limited. The obtained densities imply a severe underpopulation of the 4s state in the expansion with respect to Saha, indicating the nonequilibrium (recombining) character of the plasma.

In the supersonic region, the tendency of the gradual axial decay of the 4s densities can be modeled using the continuity equation in a quasi-one-dimensional form. Further refinement of the model could be obtained by applying more specific axial dependences of the axial velocity, the escape factor, the electron density and temperature, and the three-particle recombination coefficient.

The typical supersonic axial density drop appears to be absent for the 4s states. In the expansion, there is a substantial production of 4s states by three-particle recombination, compensating for the loss by the expansion and by radiative decay.

In the subsonic part ($z\geq87$ mm) the measured 4s densities are confirmed by a local balance model. The 4s densities appear to remain approximately constant. It

appears that the escape factor for radiative decay of the resonant states to the ground state is relatively small, of the order of 10^{-3}, and that there is production by three-particle recombination.

An uncertainty in the modeling is the value of the three-particle recombination coefficient. The actual results support the value found in Ref. [24] for argon. So when applying the general formula given by Biberman, Vorob'ev, and Yakubov [31] for the three-particle recombination in expanding thermal argon arc plasmas the coefficient has to be modified.

ACKNOWLEDGMENTS

This work was made possible by the financial support of Electricité de France, as a consequence of a collaboration with the Eindhoven University of Technology (Contract No. M60L04/7B006/EL447). Furthermore, the work of J. J. Beulens, M. Schuwer, H. M. M. de Jong, A. T. Kiers, M. J. F. van de Sande, and A. B. M. Hüsken in developing and building the spectroscopy setup, including the homemade assembly for the photodiode array, is gratefully acknowledged.

[1] G. M. W. Kroesen, Ph.D. thesis, University of Technology, Eindhoven, The Netherlands, 1988.

[2] M. C. M. van de Sanden, Ph.D. thesis, University of Technology, Eindhoven, The Netherlands, 1991.

[3] J. J. Beulens, Ph.D. thesis, University of Technology, Eindhoven, The Netherlands, 1992.

[4] A. J. M. Buuron, Ph.D. thesis, University of Technology, Eindhoven, The Netherlands, 1993.

[5] M. T. Bowers and J. B. Laudenslager, in *Principles of Laser Plasmas,* edited by G. Bekefi (Wiley, New York, 1976).

[6] M. Bourène and J. Le Calvé, J. Chem. Phys. **58**, 1452 (1973).

[7] M. C. M. van de Sanden, G. M. Janssen, J. M. de Regt, D. C. Schram, J. A. M. van der Mullen, and B. van der Sijde, Rev. Sci. Instrum. **63**, 3369 (1992).

[8] Zhou Qing, M. C. M. van de Sanden, M. J. de Graaf, D. K. Otorbaev, G. J. Meeusen, A. J. M. Buuron, and D.C. Schram, in *Proceedings of the Eleventh International Symposium on Plasma Chemistry, Loughborough, UK, 1993,* edited by J. Harry (ISPC, Loughborough, 1993), Vol. 4, p. 1374.

[9] A. J. M. Buuron, D. K. Otorbaev, J. J. Beulens, T. Kiers, M. C. M. van de Sanden, H. de Jong, and D. C. Schram, High Temp. Chem. Processes **2**, 75 (1993).

[10] E. F. M. van der Held, Z. Phys. **70**, 508 (1931).

[11] *Plasma Diagnostics,* edited by W. Lochte-Holtgreven (North-Holland, Amsterdam, 1968).

[12] A. C. G. Mitchell and M. W. Zemansky, *Resonance Radiation and Excited Atoms* (Cambridge University Press, Cambridge, 1971).

[13] I. M. Vardavas, J. Quant. Spectrosc. Radiat. Transfer **49**, 119 (1993).

[14] A. J. M. Buuron, J. J. Beulens, M. J. F. van de Sande, and D. C. Schram, Fusion Technol. **19**, 2049 (1991).

[15] J. J. Beulens, A. J. M. Buuron, and D. C. Schram, Surf. Coat. Technol. **47**, 401 (1991).

[16] G. M. W. Kroesen, D. C. Schram, A. T. M. Wilbers, and G. J. Meeusen, Contrib. Plasma Phys. **31**, 27 (1991).

[17] A. T. M. Wilbers, G. M. W. Kroesen, C. J. Timmermans, and D. C. Schram, Meas. Sci. Technol. **1**, 1326 (1990).

[18] A. T. M. Wilbers, G. M. W. Kroesen, C. J. Timmermans, and D. C. Schram, in *Proceedings of the Ninth International Symposium on Plasma Chemistry,* Pugnochiuso, Italy, 1989, edited by R. d'Agostino (ISPC, Pugnochiuso, 1989), Vol. I, p. 302.

[19] M. Haverlag, G. M. W. Kroesen, and F. J. de Hoog, in *Proceedings of the Ninth International Symposium on Plasma Chemistry* (Ref. [18]), Vol. I, p. 441.

[20] G. M. W. Kroesen, M. S. de Wit, Y. L. M. Creijghton, F. J. de Hoog, and D. C. Schram, in *Proceedings of the Ninth International Symposium on Plasma Chemistry* (Ref. [18]), Vol. I, p. 445.

[21] A. J. M. Buuron, D. K. Otorbaev, M. C. M. van de Sanden, and D. C. Schram (unpublished).

[22] R. J. Rosado, Ph.D. thesis, University of Technology, Eindhoven, The Netherlands, 1980.

[23] W. L. Wiese, M. W. Smith, and B. M. Miles, *Atomic Transition Probabilities,* Natl. Bur. Stand. Ref. Data Ser., Natl. Bur. Stand. (U.S.) Circ. No. 22 (U.S. GPO, Washington, DC, 1969).

[24] M. C. M. van de Sanden, J. M. de Regt, and D. C. Schram, Phys. Rev. E **47**, 2792 (1993).

[25] R. F. G. Meulenbroeks, P. A. A. van der Heyden, M. C. M. van de Sanden, and D. C. Schram, J. Appl. Phys. **75**, 2775 (1994).

[26] In Refs. [4] and [9] the results were presented as a function of the distance to the exit of the nozzle.

[27] H. R. Griem, *Spectral Line Broadening by Plasmas* (Academic, New York, 1974).

[28] D. P. Aeschliman, R. A. Hill, and D. L. Evans, Phys. Rev. A **14**, 1421 (1976).

[29] J. Koulidiati, A. Czernichowski, J. J. Beulens, and D. C. Schram, J. Phys. (Paris) Colloq. **18**, C5-297 (1990).

[30] J.-L. Delcroix, C. M. Ferreira, and A. Ricard, in *Principles of Laser Plasmas* (Ref. [5]).

[31] L. M. Biberman, V. S. Vorob'ev, and I. T. Yakubov, *Kinetics of Nonequilibrium Plasmas* (Plenum, New York, 1987).

[32] D. A. Benoy, J. A. M. van der Mullen, M. C. M. van de Sanden, B. van der Sijde, and D. C. Schram, J. Quant. Spectrosc. Radiat. Transfer, **49**, 129 (1993).

[33] H. W. Drawin and F. Emard, Beitr. Plasma Phys. **13**, 143 (1973).

[34] J. Batenburg, Eindhoven University of Technology Report No. VDF/NT 81-11, (unpublished).

[35] I. I. Sobelman, *Introduction to the Theory of Atomic Spectra* (Pergamon, Oxford, 1972).

[36] H. Ashkenas and F. S. Sherman, in *Rarefield Gas Dynamics,* edited by J. H. de Leeuw (Academic, New York, 1966).

[37] A. Gleizes, Beitr. Plasma Phys. **22**, 241 (1982).

[38] A. Funahashi and S. Takeda, J. Phys. Soc. Jpn. **25**, 298 (1968).

[39] J. J. Beulens, D. Milojevic, D. C. Schram, and P. M. Vallinga, Phys. Fluids B **3**, 2548 (1991).

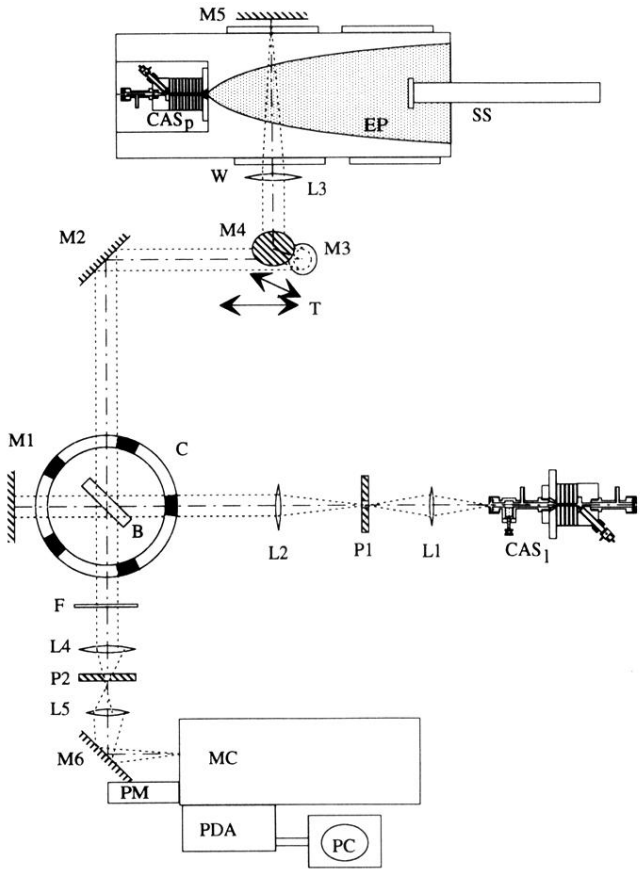

FIG. 1. The expanding cascaded arc plasma and the spectroscopy setup: CAS$_I$, cascaded arc light source; *M*, mirrors; *L*; quartz lenses; $P_{1,2}$, pinholes; *B*, beam splitter; *C*; chopper; *T*, translator; CAS$_P$, cascaded arc particles source; EP, expanding plasma; SS, movable substrate support; *W*, quartz window; *F*, order filter; MC, monochromator; PDA, photodiode array; PM, photomultiplier; PC, personal computer.

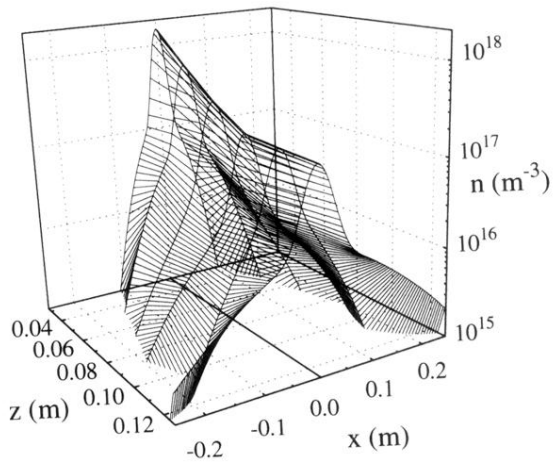

FIG. 10. Map displaying the total density of the argon 4*s* state over the entire cross section of the chamber, obtained by interpolation of the radial profiles on the six measurement positions.

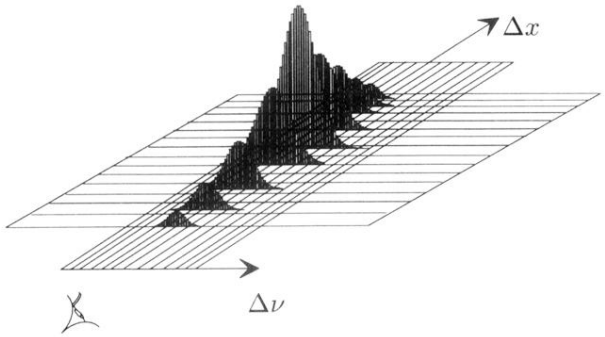

FIG. 4. Grid for integrating the absorption over the frequency ν and over a line of sight (with running coordinate x).